Surface reactivity of hydroxyapatite nanocoatings deposited on iron oxide magnetic spheres towards toxic metals

Huihui Yang,[a,b] Sylvie Masse,[a] Hao Zhang,[b] Christophe Hélary,[a] Laifeng Li,[b] Thibaud Coradin[a,*]

[a]UPMC Univ Paris 06 ; CNRS, Chimie de la Matière Condensée de Paris, Collège de France, 11 place Marcelin Berthelot, F-75005 Paris, France. E-mails: sylvie.masse@upmc.fr, christophehelary@hotmail.com, thibaud.coradin@upmc.fr

[b]Key Laboratory of Cryogenics, Technical Institute of Physics and Chemistry, Chinese Academy of Sciences, Beijing 100190, People Republic of China. E-mails: hhyanghh@gmail.com, stavrosatic@gmail.com, laifengli@mail.ipc.ac.cn

* **Corresponding author**. E-mail: thibaud.coradin@upmc.fr; tel: +33-144271528; fax: +33-144271443

Abstract

Hypothesis
Hydroxyapatite and magnetite are two environmentally-friendly mineral phases that have fruitful properties for remediation process. The formation of magnetic core@sorbent shell nanostructures should provide efficient materials for toxic metal removal from aqueous media. However the nanoscale confinement of hydroxyapatite may influence its reactivity.

Experiments
Fe_3O_4@Hydroxyapatite nanocomposites were prepared by surface-controlled precipitation of hydroxyapatite layers from 10 nm to 150 nm in thickness on iron oxide spheres. The surface reactivity of the core-shell particles towards selected inorganic ions of environmental relevance (Pb(II), Y(III), Eu(III), Sb(III)) was studied by batch sorption experiments, X-ray diffraction and electron microscopy.

Findings
The reactivity of the hydroxyapatite coating varied from partial cation exchange to dissolution/transformation of the shell. The nature and extent of the reactions depended significantly on the hydroxyapatite layer structure but was not significantly influenced by the magnetic core. These novel nanocomposites should be useful for environmental applications.

Keywords: Hydroxyapatite; Iron oxide; Nanocomposites; Magnetic recovery; Remediation

1. Introduction

Hydroxyapatite $Ca_{10}(PO_4)_6(OH)_2$ is a mineral phase of complex reactivity [1-3]. Such a complexity makes it a versatile material, especially for application in the biomedical field [4,5] and in remediation technologies [6,7]. The latter applications are related to its well-known ability to immobilize divalent and tri-valent metal ions, either by partial cationic exchange with calcium ions or via a dissolution/reprecipitation reaction [8-12]

Recently, the possibility to combine the properties of hydroxyapatite with other inorganic phases within core-shell nanostructures has attracted great attention. For instance, lanthanide-doped hydroxyapatite/silica [13], hydroxyapatite/TiO_2 [14] and hydroxyapatite/cobalt ferrite [15] core-shell nanoparticles have been studied for fluorescence imaging, photocatalytic processes and drug delivery, respectively. The association of hydroxyapatite with iron oxide particles provides a promising method to design sorbents that combines large sorption capacities and easy recovery via magnetic separation [16,17]. Hence several iron oxide-hydroxyapatite nanocomposites have been described in the literature [18-24]. However, the surface reactivity of apatite nanocoatings towards metal ions has never been studied, despite its primary importance for applications of these materials in remediation processes.

With this purpose, we have prepared here core-shell Fe_3O_4@Hydroxyapatite spheres with various coating thicknesses. These well-defined objects allowed the detailed study of the surface reactivity towards metals that were selected for their environmental relevance as well as for their different sizes, charge and reactivity: Pb(II), a widespread metal pollutant [25] whose interactions with hydroxyapatite has been widely studied [8-10], Y(III) and Eu(III), belonging to the rare-earth family that has recently attracted great attention in terms of resource and environmental impact [26] and Sb(III), a metal major concern worldwide [27]. A diversity of behaviors ranging from partial cation exchange to full transformation of the

hydroxyapatite structure was observed. The thickness of the coating was shown to impact on its exchange capacity towards rare earth cations. The contribution of the iron oxide core to the metal-particle interactions was only observed for Sb(III) species. Taken together, these data suggest that these novel core-shell nanoparticles have a high potentiality in environmental applications.

2. Experimental section

2.1. Preparation of Fe_3O_4@Hydroxyapatite nanospheres

The synthesis of Fe_3O_4 spheres was performed according to a previously described procedure [28]. $FeCl_3.6H_2O$ (4.275 g, 17.5 mmol) was dissolved in ethylene glycol (140 mL) until a clear solution was obtained. Sodium acetate (12.6 g) and polyethylene glycol (3.5 g) were then added and the mixture was vigorously stirred for 30 min. The solution was transferred into teflon-lined stainless-steel autoclaves that were sealed and maintained at 200 °C for 10 h. After cooling, the recovered dark powder was washed several times with ethanol. The hydroxyapatite coating procedure was adapted from previous reports and summarized in Scheme 1 [15,29]. In a first step, 1 g of the iron oxide spheres was dispersed into 35 mL of a 1 M L-aspartic acid solution at 80 °C for 2 h, then washed with water (sample FeA). The recovered particles were then dispersed in 100 mL of a 0.06 M (sample $FeAH_1$) or 0.03 M (sample $FeAH_2$) $NH_4H_2PO_4$ solution. A 100 mL ethanol-water (50:50% v/v) solution 0.10 M ($FeAH_1$) or 0.05 M ($FeAH_2$) in $Ca(OH)_2$ was prepared in parallel and slowly added to the particle suspension over a period of 24 h. The resulting powder was recovered by magnetic separation, washed with deionized water and dried at 80 °C under vacuum overnight. A reference hydroxyapatite sample HAp was prepared in the same conditions except for the absence of FeA in the $NH_4H_2PO_4$ solution.

2.2. Metal-surface interactions

Metal ion solutions with concentrations varying from 0 to 1000 mg.L^{-1} were prepared from $Pb(NO_3)_2.6H_2O$, $Y(NO_3)_3.6H_2O$, $Eu(NO_3)_3.6H_2O$ and $KSbC_4H_4O_7.0.5H_2O$ salts dissolved in deionized water adjusted with HCl at pH 5, 6, 6 and 4, respectively, to ensure full dissolution. Kinetics studies were performed in 500 mL glass flasks by adding 0.1 g of the FeAH1 powder to 200 mL of the metal solutions. Batch removal experiments were conducted in 200 mL glass flasks by adding 0.1 g of the different powders to 50 mL of the metal solutions. The suspension was stirred at 200 rpm over 24 h at 25°C to reach sorption equilibrium. After magnetic separation, the concentrations of Pb, Y, Eu, Sb in the aqueous phase and the elemental composition of the sorbents (after dissolution in HCl) were determined by inductively coupled plasma (ICP) spectrophotometry (Varian 710-ES). Each experiment was replicated four times.

2.3. Powder characterization

Powder X-ray diffraction (XRD) was performed on a Philips PW131 diffractometer using Cu Kα radiation. Particle size and charge were measured using dynamic light scattering (DLS) and zeta potential (ζ) measurements using a Brookhaven zeta Plus apparatus. Observation were performed by transmission electron microscopy (TEM) on a JEOL JEM-2100F operating at 200 kV and scanning electron microscopy (FEG-SEM) on a Hitachi SU70 with energy-dispersive spectrometry (EDX) operating at 5 kV. The magnetic properties were measured using a vibrating sample magnetometer (VSM) Lake Shore 7410 in an applied magnetic field of ± 20 kOe at room temperature.

3. Results and discussion

3.1. Preparation and characterization of Fe_3O_4@Hydroxyapatite spheres

The iron oxide spheres before and after hydroxyapatite coating were first observed by SEM. The initial spheres have diameters ranging between 100 nm and 500 nm and consist of aggregated nanoparticles, *ca*. 10-20 nm in diameter (Fig. 1 and Supporting Information). After mineralization, a layer is deposited on their surface, with protruding rod-like crystals being evidenced for $FeAH_1$. TEM allows a more detailed observation of the mineral shell, with crystals adopting a flat configuration on the iron oxide surface (thickness *ca*. 10 nm) for $FeAH_2$ and a sunflower-like corona (thickness *ca*. 150 nm) for $FeAH_1$ (Fig. 2 and Supporting Information). DLS analyses indicate that bare magnetite, L-aspartic acid-coated particles (FeA) and $FeAH_2$ have a very similar size distribution (average size: 450 nm; s.d.: 30 nm)) whereas $FeAH_1$ particles are larger (average size: 570 nm; s.d.: 30 nm). Zeta potential ζ is -20 ± 2 mV for Fe_3O_4 and decreases to -27 ± 2 mV for FeA, confirming L-aspartic adsorption. After mineralization, ζ rises to -21 mV ± 2 mV for $FeAH_1$ and $FeAH_2$, as expected from the negative charge of hydroxyapatite near neutral pH.

XRD patterns of the materials confirm that the spheres are composed of magnetite Fe_3O_4, as indicated by diffraction peaks at 2θ = 30.2°, 35.5°, 43.2°, 53.1°, 57.1°, and 62.9° from the (220), (311), (400), (422), (511) and (440) lattice planes (Fig. 3). These peaks are retained in the composites, together with new peaks at 2θ = 25.9°, 31.8°, 32.2°, 32.9°, 34.1°, 39.8°, 46.7 ° and 49.5° corresponding to the (002), (211), (112), (300), (202), (310), (222) and (213) planes of hydroxyapatite $Ca_{10}(PO_4)_6(OH)_2$.

ICP analysis of the dissolved powders (Table 1) indicates that the experimental Ca/P molar ratio is 1.63 ± 0.05 and 1.70 ± 0.05 for $FeAH_1$ and $FeAH_2$, respectively, close to the stoichiometric ratio (1.67) of HAp. Furthermore, the Fe/P molar ratio is 2.15 ± 0.05 for $FeAH_1$ and 4.15 ± 0.05 for $FeAH_2$, in reasonable agreement with the calculated Fe/P molar

ratios from the synthesis, *i.e*. 2 and 4 respectively. As the analyzed powder was recovered by magnetic separation, it implies that hydroxyapatite precipitation occurred almost completely on the surface of Fe_3O_4 particles.

The magnetic properties of the pure magnetite and $FeAH_1$ composite were recorded at room temperature. As shown in Fig. 4, the two curves present extremely low coercivity and remanence, meaning that the powders exhibit a superparamagnetic behavior. This is expected for the 10 nm-large magnetite nanoparticles forming the spheres [28], and the hydroxyapatite shell has no effect on this behavior. The $FeAH_1$ has a saturation magnetization (*Ms*) of 43.9 $emu.g^{-1}$, which is *ca*. 49 % of that of pure magnetite (89.9 $emu.g^{-1}$) [30], in agreement with the composition of this sample, *i.e*. with a Fe_3O_4:HAp weight ratio of 1:1.

3.2. Surface reactivity of Fe_3O_4@Hydroxyapatite nanospheres

To investigate the surface properties of the apatite layer in detail, four inorganic species of environmental relevance and exhibiting various chemical properties were selected. Samples were designated as Pb-, Y-, Eu-, and Sb- groups.

In a first step, interactions between metal ions and the composite $FeAH_1$ powder were investigated via kinetics studies. Two different behaviors were observed depending on the considered inorganic species. For Y and Eu, a fast reduction in the metal content of the solution was observed within *ca*. 2 h and a plateau as reached after 6-7 h (Fig. 5a). For Pb and Sb, the depletion process was also very fast in the first hour of contact and then proceeded more slowly but continuously over a 24 h (Fig. 5b). This trend was particularly evident for antimony. These first results suggest that the reaction responsible for metal removal from solution in the case of Pb and Sb is not a simple adsorption processes.

To investigate further the metal-composite interactions, the removal ability of the different materials was studied as a function of metal concentration after a 24 h contact time. The

removal of lead ion from aqueous solutions was first studied. As shown in Fig. 6a, a very efficient depletion in Pb(II) was observed for HAp, $FeAH_1$ and $FeAH_2$ followed by a plateau at 1.20 ± 0.01 $mmol.g^{-1}$, 1.55 ± 0.01 $mmol.g^{-1}$ and 1.30 ± 0.01 $mmol.g^{-1}$, respectively. Noticeably, the pure magnetite spheres did not show any significant effect on lead depletion. As shown in Fig. 7a, after contact with the Pb(II) solution, new peaks are present in the XRD patterns of both Pb-$FeAH_1$ and HAp, that could be attributed to the formation of hydroxypyromorphite $Pb_{10}(PO_4)_6(OH)_2$. In parallel, SEM imaging demonstrates the presence of micron-size acicular crystals associated with the composite particles, that were also observed in the Pb-HAp sample (Fig. 8a,b). EDX analysis of these crystals shows high P and Pb content and only traces of Ca (Supporting Information), in agreement with the precipitation of hydroxypyromorphite $Pb_{10}(PO_4)_6(OH)_2$.

As already well-documented in the literature [8,31], this reaction can occur in a two-step process involving the surface dissolution of hydroxyapatite that releases phosphate and hydroxyl ions (Eq. 1), followed by hydroxypyromorphite precipitation (Eq. 2):

$$Ca_{10}(PO_4)_6(OH)_2 + 3\ H_2O = 10\ Ca^{2+} + 6\ HPO_4^{2-} + 8\ OH^- \quad (1)$$

$$10\ Pb^{2+} + 6\ HPO_4^{2-} + 8\ OH^- = Pb_{10}(PO_4)_6(OH)_2 + 3\ H_2O \quad (2)$$

The occurrence of this reaction is supported by the fact that the final (Ca+Pb)/P molar ratio, as obtained by ICP, do not significantly vary from the initial Ca/P ratios in the HAp and composite structures (Table 1). In addition the (Ca+Pb)/Fe ratio is similar to the initial Ca/Fe ratio, indicating that the precipitation process is occurring at the magnetic sphere surface without perturbation of the core material. It is interesting to calculate the lead removal capacity of the materials per g of hydroxyapatite. The obtained values are 1.2, 3.6 and 3.9

mmol.g^{-1} for HAp, $FeAH_1$ and $FeAH_2$, respectively, suggesting a larger surface reactivity of the hydroxyapatite coatings in the composites compared to the HAp powder.

The isotherms of Y(III) removal showed a similar trend as Pb(II) ones, *i.e*. large depletion at low yttrium amount followed by a plateau (Fig. 6b). The maximum removal is obtained with HAp (1.88 ± 0.01 mmol.g^{-1}). The composites show close reactivity (1.05 ± 0.01 mmol.g-^{1} and 0.89 ± 0.01 mmol.g^{-1}). However, no new peak was evidenced on the XRD pattern after adsorption (Fig. 7b), and no additional precipitation was observed by SEM (Fig. 8c and Supporting Information). The ICP data indicates a (Ca+Y)/P molar ratio of *ca*. 1.5 (Table 1) indicating that the underlying process is not limited to Y(III) adsorption, that would lead to an increase of this ratio compared to the initial Ca:P value, but rather suggests an ionic exchange between Ca(II) and Y(III) (eq. 4):

$$Ca_{10}(PO_4)_6(OH)_2 + x\ Y^{3+} = Ca_{10-(3/2)x}Y_x(PO_4)_6(OH)_2 + (3/2)x\ Ca^{2+} \quad (4)$$

Taking into account that the magnetite particles alone did not exhibit any Y(III) sorption capacity, the removal capacity per g of HAp can also be calculated from the plateau of the isotherms. This leads to 1.9 mmol.g-^{1}, 2.1 mmol.g-^{1} and 2.6 mmol.g-^{1}for HAp, $FeAH_1$ and $FeAH_2$. In this situation, the exchange capacity of the hydroxyapatite structure is not significantly modified within the $FeAH_1$ composite but increases for $FeAH_2$.

A similar ion exchange is expected to occur in the presence of Eu(III) (eq. 5):

$$Ca_{10}(PO_4)_6(OH)_2 + x\ Eu^{3+} = Ca_{10-(3/2)x}Eu_x(PO_4)_6(OH)_2 + (3/2)x\ Ca^{2+} \quad (5)$$

Eu(III) removal was observed in solution for HAp and the two composites (Fig. 6c), but not for Fe_3O_4. No additional peak was identified on the corresponding XRD patterns (Fig. 7b) and no additional phase was observed by SEM (Supplementary Information). Removal efficiency was 1.25 ± 0.01, 0.85 ± 0.01 and 1.10 ± 0.01 $mmol.g^{-1}$ for HAp, $FeAH_1$ and $FeAH_2$, respectively, corresponding to removal capacities per g of hydroxyapatite of *ca*. 1.2, 1.7 and 3.3 $mmol.g^{-1}$. This confirms the results obtained with Y(III) suggesting that the thin hydroxyapatite coating of $FeAH_2$ is more suitable for rare-earth incorporation than the thicker coating of $FeAH_1$, both of which being more reactive than the HAp powder.

A different situation was met when the different powders were added to the Sb(III) solutions. Antimony removal was observed for all materials, including Fe_3O_4 spheres, but the process was more progressive than for the previous metallic species (Fig. 6d). HAp and $FeAH_1$ showed similar efficiency whereas $FeAH_2$ had a distinctly lower removal ability. XRD data indicate that the magnetite structure was not modified by the presence of Sb(III) species (Fig. 7a), suggesting that the antimony-iron oxide interaction corresponds to surface adsorption. In contrast, the characteristic peaks of the hydroxyapatite structure disappeared almost entirely for HAp and $FeAH_1$ and new peaks corresponding to Sb_2O_3 (senarmontite phase) were present. An additional peak at $2\theta = 11.5°$ was attributed to $CaHPO_4$ although it is not possible to firmly confirm this attribution. In parallel, ICP indicates a very significant increase of the (Ca+Sb)/P molar ratio and, more remarkably, of the Fe/P molar ratio indicating a complete modification of the mineral phase composition and confirming the disappearance of the hydroxyapatite coating (Table 1). Accordingly, SEM imaging indicate the presence of large crystalline particles, up to 20 μm in length, coated with spherical particles whose size corresponds to the magnetite spheres (Fig. 8e,f and Supplementary Information)

The Sb(III) has a strong tendency to hydrolyze, resulting in the formation of SbO^+, $Sb(OH)_3$ and $Sb(OH)_4^-$ [32]. These are the predominant Sb species in the solution over the pH range used in our experiments. Based on the literature [33], it is possible to propose that after hydroxyapatite dissolution (eq. 6), the following reaction occurs:

$$3\ Ca^{2+} + 3\ HPO_4^{2-} + 4\ SbO^+ + 4\ OH\text{-} = 3\ Ca(HPO_4) + 2\ Sb_2O_3 + 2\ H_2O \quad (6)$$

Combined with eq. 1, one obtains the following reaction (eq. 7):

$$Ca_{10}(PO_4)_6(OH)_2 + x\ SbO^+ + x/4\ H_2O = x/2\ Sb_2O_3 + 3x/4\ Ca(HPO_4) + (1\text{-}x/8)Ca_{10}(PO_4)_6(OH)_2 + x/2\ Ca^{2+} \quad (7)$$

In the case of HAp, the maximum removal is 4.00 ± 0.02 $mmol.g^{-1}$. For $FeAH_1$ and $FeAH_2$, the maximum removal efficiency is 4.00 ± 0.02 $mmol.g^{-1}$ and 1.00 ± 0.02 $mmol.g^{-1}$ but this value may include Sb(III) sorption on iron oxide. However, magnetite particles alone remove 0.33 ± 0.02 $mmol.g^{-1}$ of antimony species. Therefore Sb removal by the hydroxyapatite layer should be *ca*. 7.6 mmol and 2.6 mmol per g. These values can be converted into $Sb/Ca_{10}(PO_4)_6(OH)_2$ molar ratios that correspond to *x* values in eq. 7. This leads to x = 4, 7.6 and 2.5 for HAp, $FeAH_1$ and $FeAH_2$ respectively. Noticeably, eq. 7 indicates that hydroxyapatite is completely converted into Sb_2O_3 and $Ca(HPO_4)$ for x = 8. Therefore it is expected that the hydroxyapatite coating of $FeAH_1$ is almost fully converted into $Ca(HPO_4)$ in the presence of Sb(III), in agreement with the XRD data and SEM images.

Overall three different situations are met. For lead ions, a surface reaction takes place where dissolution of hydroxyapatite occurs and the released hydroxyl and phosphate ions interact with Pb^{2+} to precipitate hydroxypyromorphite. In this situation, $FeAH_1$ and $FeAH_2$

behave similarly and are more reactive than HAp. This can be related to the lowest crystallinity of the hydroxyapatite coatings compared to bulk HAp, that makes them more prone to dissolution. For the two rare-earth (RE) ions, a substitution of calcium ions by Eu(III) and Y(III) in the apatite structure is evidenced. In this situation HAp and $FeAH_1$ show similar behavior whereas $FeAH_2$ shows higher substitution rate. This reaction should involve both RE ion diffusion to the surface of the hydroxyapatite crystals and their solid-state substitution. The former should be sensitive to the accessibility of the mineral surface. It can therefore be suggested that the dense organization of hydroxyapatite crystals on the iron oxide particles observed for $FeAH_1$ by TEM limits the ionic diffusion through the whole coating thickness whereas RE^{3+} have easy access to the whole hydroxyapatite surface in the flat coating of $FeAH_2$. This hypothesis is strengthened by the fact that the difference between the two composites is more particularly significant for Eu(III) ions, that have a larger ionic radius than Y(III).

Finally, in the case of Sb(III), the surface dissolution of hydroxyapatite leads to OH^- release that induces the precipitation of Sb_2O_3 and the acidification of the medium. In this condition, $CaHPO_4$ is the most stable calcium phosphate phase. In the case of $FeAH_1$, this reaction proceeds until almost entire coating dissolution. The lowest conversion is observed for $FeAH_2$ and HAp represents an intermediate situation. Whereas the difference between $FeAH_1$ and HAp can also be related to faster dissolution due lower crystallinity, the poor reactivity of $FeAH_2$ is more difficult to understand. One possible explanation is that the precipitation phenomenon, as observed by SEM, reduces the accessibility of the particle surface. In parallel it must be noticed that this is the only situation where the metal species also interact with the iron oxide surface so that some competition may exist between SbO^+-Fe_3O_4 and SbO^+-HAp interactions.

4. Conclusions

The association of iron oxide and hydroxyapatite at the nanoscale leads to magnetically-recoverable core-shell particles exhibiting strong affinity for several metallic species. The ability of these particles to remove toxic species from aqueous solutions is equivalent if not greater than the hydroxyapatite alone, as an effect of the lower crystallinity and higher surface accessibility of the calcium phosphate coating. In only one situation (*i.e.* SbO^+) did the iron oxide core was involved in the nanocomposite reactivity. Hence the ability to combine magnetic and sorbent materials within single objects appears as a promising route to design efficient colloidal systems for remediation. In particular, the formation of hydroxyapatite nanocoatings on large iron oxide beads is advantageous compared to hydroxyapatite nanoparticles as it limits aggregation phenomena that decrease the accessible reactive surface [34] and it also provides a product that is more easily and safely handled [35]. In addition, compared to previous reports, the dimensions of the two phases can be easily tuned [16,20-22]. Indeed, these nanocomposite powders should now be evaluated with more realistic contaminated waters, not only to evaluate their potential for application but also to investigate further the complexity of the hydroxyapatite nanolayers reactivity.

Acknowledgments

H. Yang and L. Li acknowledge funding support from the National Natural Science Foundation of China (Grant No. 51107139) and the National Magnetic Confinement Fusion Science Program (Grant No. 51077123). The authors thank P. Le Griel (LCMCP), P. Beaunier (Laboratoire de Réactivité de Surface, UPMC) and D. Montero (Institut des Matériaux de Paris Centre, UPMC) for electron microscopy imaging

Appendix A. Supplementary material

Supplementary data associated with this article can be found, in the online version, at http://dx.doi.org/10.1016/xxxx.

References

[1] J.C. Elliott, Structure and chemistry of apatites and other calcium orthophosphates, Elsevier, Amsterdam, 1994.

[2] C. Rey, C. Combes, C. Drouet, H. Sfihi, A. Barrough, Physico-chemical properties of nanocrystalline apatites: implications for biominerals and biomaterials. Mater. Sci. Eng., C 27 (2007) 198-205.

[3] A. Bengtsson, A. Shchukarev, P. Persson, S.A. Sjöberg, A solubility and surface complexation study of a non-stoichiometric hydroxyapatite. Geochim. Cosmochim. Acta 73 (2009) 257-267.

[4] R.Z. Legeros, Calcium phosphates in oral biology and medicine, in: Monographs in Oral Science, Vol. 15, H. Meyer (Ed), Karger, Basel, 1991.

[5] M. Epple, K. Gensan, R. Heumann, J. Klesing, A. Kotvun, S. Neumann, V. Sokolova, Application of calcium phosphate nanoparticles in biomedicine. J. Mater. Chem. 20 (2010) 18-23.

[6] A. Dybowska, D.A.C. Manning, M.J. Collins, T. Wess, S. Woodgate, E. Valsami-Jones, An evaluation of the reactivity of synthetic and natural apatites in the presence of aqueous metals. Sci. Tot. Environ. 407 (2009) 2953-2965.

[7] A. Nzihou, P. Sharrock, Role of phosphate in the remediation and reuse of heavy metal polluted wastes and sites. Waste Biomass. Valor. 1 (2010) 163-174.

[8] Q.Y. Ma, S.J. Traina, T.J. Logan, J.A. Ryan, In-situ lead immobilization by apatite. Environ. Sci. Technol. 27 (1993) 1803-1810.

[9] X. Cao, L.Q. Ma, D.R. Rhue, C.S. Appel, Mechanisms of lead, copper, and zinc retention by phosphate rock. Environ. Pollution 131 (2004) 435-444.

[10] M. Mouflih, A. Aklil, S. Sebtib, Removal of lead from aqueous solutions by activated phosphate, J. Hazard. Mater. B119 (2005) 183-188.

[11] Z. Elouear, J. Bouzid, N. Boujelben, M. Feki, F. Jamoussi, A. Montiel, Heavy metal removal from aqueous solutions by activated phosphate rock, J. Hazard. Mater. 156 (2007) 412-420.

[12] S. Saoiabi, A. Laghzizil, A. Saoiabi, J.L. Ackerman, T. Coradin, Lead and zinc removal from aqueous solutions by aminotriphosphonate-modified converted natural phosphates. Chem. Engin. J. 211-212 (2012) 233-239.

[13] M. Neumeier, L.A. Hails, S.A. Davis, S. Mann, M. Epple, Synthesis of fluorescent core–shell hydroxyapatite nanoparticles. J. Mater. Chem. 21 (2011) 1250-1254.

[14] F. Shi, Y. Li, H. Wang, Q. Zhang, Fast synthesis of rutile/apatite core/shell structured photocatalyst in simulated body fluid. Adv. Mater. Res. 465 (2012) 66-71.

[15] I.M. Tang, N. Krishnamra, N. Charoenphandhu, R. Hoonsawat, W. Pon-On, Biomagnetic of apatite-coated cobalt ferrite: a core–shell particle for protein adsorption and pH-controlled release. Nanoscale Res. Lett. 6 (2011) 19.

[16] L. Dong, Z. Zhu, Y. Qiu, J. Zhao, Removal of lead from aqueous solution by hydroxyapatite/magnetite composite adsorbent. Chem. Engin. J. 165 (2010) 827-834.

[17] P. Xu, G.M. Zeng, D.L. Huang, C.L. Feng, S. Hu, M. H. Zhao, C. Lai, Z. Wei, C. Huang, G.X. Xie, Z.F. Liu, Use of iron oxide nanomaterials in watsewater treatment: a review. Sci Total Environ. 424 (2012) 1-10.

[18] C.H. Hou, S.M. Hou, Y.S. Hsueh, J. Lin, H.C. Wu, F.H. Lin, The in vivo performance of biomagnetic hydroxyapatite nanoparticles in cancer hyperthermia therapy. Biomaterials 30 (2009) 3956-3960.

[19] D. Wang, X. Duan, J. Zhang, A. Yao, L. Zhou, W. Huang, Fabrication of superparamagnetic hydroxyapatite with highly ordered three-dimensional pores. J. Mater. Sci. 44 (2009) 4020-4025.

[20] Z. Yang, X. Gong, C. Zhang, Recyclable Fe_3O_4/hydroxyapatite composite nanoparticles for photocatalytic applications. Chem. Engin. J. 165 (2010) 117-121.

[21] A. Mir, D. Mallik, S. Bhattacharya, D. Mahata, A. Sinha S. Nayar, Aqueous ferrofluids as templates for magnetic hydroxyapatite nanocomposites. J. Mater. Sci.:Mater. Med. 21 (2010) 2365-2369.

[22] E.B. Ansar, A. Yokogowa, W. Wunderlich, V. Varma, Synthesis and characterization of iron oxide embedded hydroxyapatite bioceramics. J. Am. Ceram. Soc. 95 (2012) 2695-2699.

[23] R.K. Singh, A.M. El-Fiqui, K.D. Patel, H.W. Kim, A novel preparation of magnetic hydroxyapatite nanotubes. Mater. Lett. 75 (2012) 130-133.

[24] E.M. Muzquiz-Ramos, D.A. Cortés-Hernandez, J. Escobedo-Bocardo, A. Zugasti-Cruz, X.S. Ramirez-Gomez, J.G Osuna-Alarcon, In vitro and in vivo biocompatibility of apatite-coated magnetite nanoparticles for cancer therapy. J. Mater. Sci.:Mater. Med. 24 (2013) 1035-1041.

[25] P. Karrari, O. Merhpour, M. Abdollahi, A systematic review on status of lead pollution and toxicity in Iran; Guidance for preventive measures, DARU Journal of Pharmaceutical Sciences 20 (2012) 1-17.

[26] A.A. Volokh, B.A. Gundorina, B.A. Revich, M.V. Frontasyeva, C.S. Pal, Phosphorus fertilizer production as a source of rare-earth elements pollution of the environment. Sci. Total. Environ. 95 (1990) 141-148.

[27] M. He, X; Wang, F. Wu, Z. Fu, Antimony pollution in China, Sci. Total Environ. 421-422 (2012) 41-50.

[28] H. Deng, X.L. Li, Q. Peng, X. Wang, J.P. Chen, Y.D. Li, Monodisperse magnetic single-crystal ferrite microspheres. Angew. Chem. Int. Ed. 44 (2005) 2782-2785.

[29] L. El Hammari, H. Merroun, T. Coradin, S. Cassaignon, A. Laghzizil, Mesoporous hydroxyapatites prepared in ethanol-water media: Structure and surface properties. Mater. Chem. Phys. 104 (2007) 448-453.

[30] M.A. Vergés, R. Costo, A.G. Roca, J.F. Marco, G.F. Goya, C.J. Serna, M.P. Morales, Uniform and water stable magnetite nanoparticles with diameters around the monodomain-multidomain limit. J. Phys. D : Appl. Phys. 41 (2008) 134003.

[31] S.K. Lower, P.A. Maurice, S.J. Traina, E.H. Carlson, Aqueous Pb sorption by hydroxylapatite: Application of atomic force microscopy to dissolution, nucleation, and growth studies. Am. Mineral. 83 (1998) 147-158.

[32] H. Hashimoto, T. Nishimura, Y. Umetsu, Hydrolysis of Antimony(III)-hydrochloric acid solutions at 25°C. Mater. Trans. 44 (2003) 1624-1629.

[33] Q.H. Li, S.W. Xiao, Z.H. Liu, X.Y. Guo, D.M. Zhang, Template effect of tartrate ion on the morphology of antimony trioxide. Chem. J. Chinese U. 21 (2000) 1344-1347.

[34] H. Bouyarmane, S. El Asri, A. Rami, C. Roux, M. A. Mahly, A. Saoiabi, T. Coradin, A. Laghzizil, Pyridine and phenol removal using natural and synthetic apatites as low cost sorbents: influence of porosity and surface interactions J. Hazard Mater. 181 (2010) 736-741.

[35] B. Karn, T. Kuiken, M. Otto, Nanotechnology and in situ remediation: a review of the benefits and risks. Environ. Health Perspect. 117 (2009) 1813-1831

Table 1. Molar ratio of various elements in the different samples before and after contact with metal ions (M = Pb, Y, Eu or Sb) as determined by ICP analyses. Values are given with a ± 0.05 error.

	[Ca + M] : P	Fe : P	[Ca + M] : Fe
HAp	1.67	-	-
Pb-HAp	1.68	-	-
Y-HAp	1.46	-	-
Eu-HAp	1.52	-	-
Sb-HAp	4.68	-	-
$FeAH_1$	1.63	2.15	0.75
Pb-$FeAH_1$	1.71	2.21	0.74
Y-$FeAH_1$	1.46	1.97	0.74
Eu-$FeAH_1$	1.66	2.27	0.73
Sb-$FeAH_1$	7.22	5.37	1.34
$FeAH_2$	1.71	4.15	0.41
Pb-$FeAH_2$	1.73	4.27	0.41
Y-$FeAH_2$	1.50	4.03	0.39
Eu-$FeAH_2$	1.60	4.02	0.39
Sb-$FeAH_2$	2.98	6.10	0.49

Scheme 1. Synthetic pathway to Fe_3O_4@Hydroxyapatite spheres

Fig. 1. SEM images of (a) as-synthesized iron oxide particles, (b) $FeAH_2$ and (c,d) $FeAH_1$ (scale bar = 500 nm except for (d) = 200 nm)

Fig. 2. TEM images of (a) HAp, (b) Fe_3O_4, (c) $FeAH_2$ and (d) $FeAH_1$ (scale bar = 100 nm except for (b) = 200 nm)

Fig. 3. XRD patterns of Fe_3O_4 spheres, $FeAH_2$, $FeAH_1$ and HAp. Characteristic diffraction peaks of (○) Fe_3O_4, (□) $Ca_{10}(PO4)_6(OH)_2$.

Fig. 4. Magnetization curves at 298 K of Fe_3O_4 and $FeAH_1$.

Fig. 5. Kinetics of metal removal (q_e) from aqueous solutions in mmol of (a) Y(III) and Eu(III) and (b) Pb(II) and Sb(III) per g of $FeAH_1$.

Fig. 6. Metal removal (q_e) from aqueous solutions in mmol of (a) Pb(II), (b) Y(III), (c) Eu(III) and (d) Sb(III) per g of HAp, $FeAH_1$, $FeAH_2$ and Fe_3O_4.

Fig. 7. XRD patterns of powders after contact with (a) Pb(II), Sb(III) and (b) Y(III), Eu(III) Characteristic diffraction peaks of (○) Fe_3O_4, (□) $Ca_{10}(PO_4)_6(OH)_2$, (③) $Pb_{10}(PO_4)_6(OH)_2$, (◆) senarmontite Sb_2O_3, (◇) $CaHPO_4$. The XRD of HAp was added on (b) for sake of clarity.

Fig. 8. SEM (except (d), TEM) images of (a) Pb-HAp, (b) Pb-$FeAH_1$, (c) Y-$FeAH_1$, (d) Eu-$FeAH_1$, (e) Sb-HAp and (f) Sb-$FeAH_1$

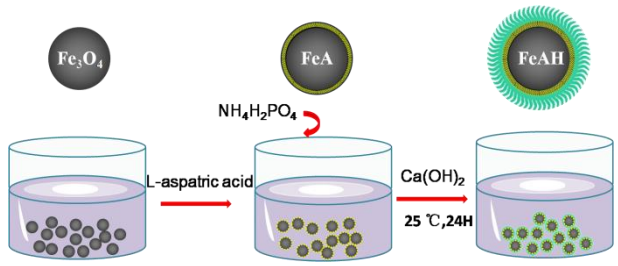

Scheme 1

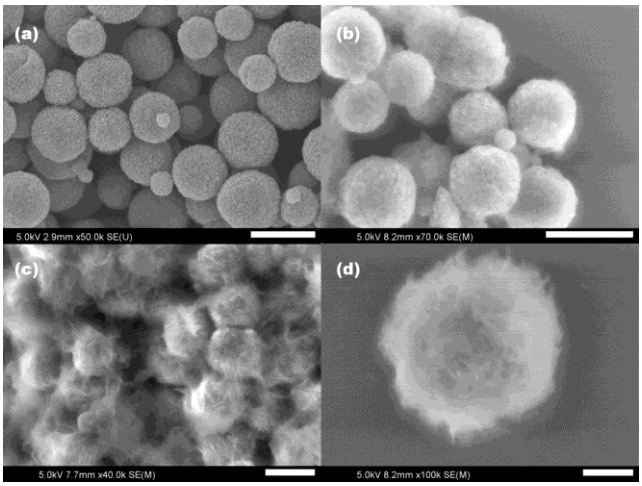
(a)
5.0kV 2.9mm x50.0k SE(U)
(b)
5.0kV 8.2mm x70.0k SE(M)
(c)
5.0kV 7.7mm x40.0k SE(M)
(d)
5.0kV 8.2mm x100k SE(M)

Fig. 1

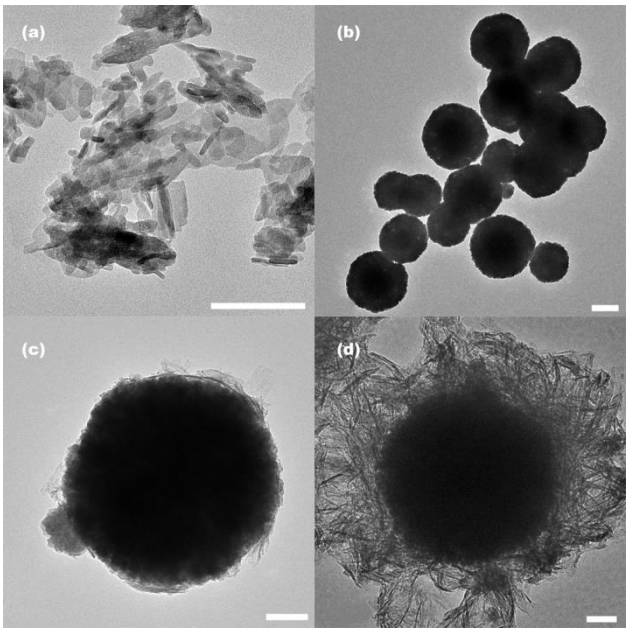

Fig. 2

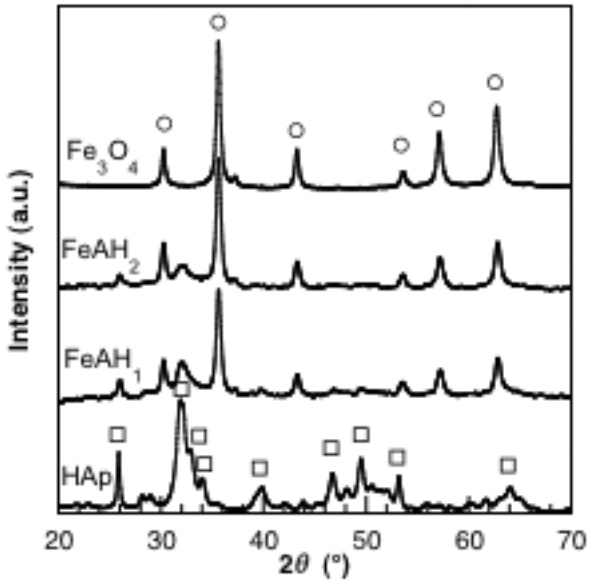

Fig. 3

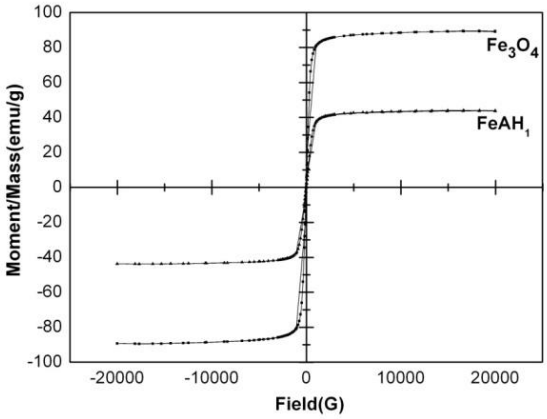
Moment/Mass(emu/g)
Field(G)
Fe3O4
FeAH1
100
80
60
40
20
0
-20
-40
-60
-80
-100
-20000
-10000
0
10000
20000

Fig. 4

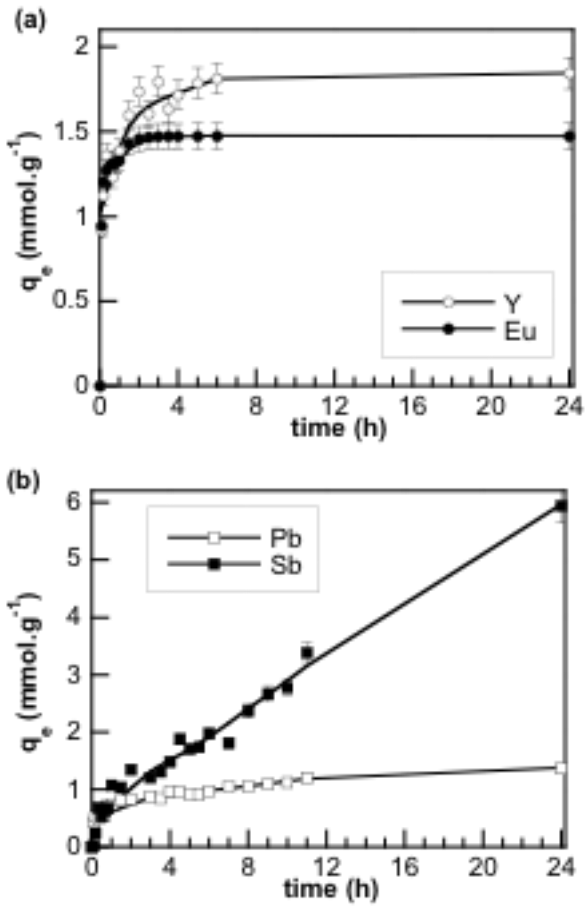
(a)
2
1.5
1
0.5
0
q_e (mmol.g^{-1})
0
4
8
12
16
20
24
time (h)
Y
Eu
(b)
6
5
4
3
2
1
0
q_e (mmol.g^{-1})
0
4
8
12
16
20
24
time (h)
Pb
Sb

Fig. 5

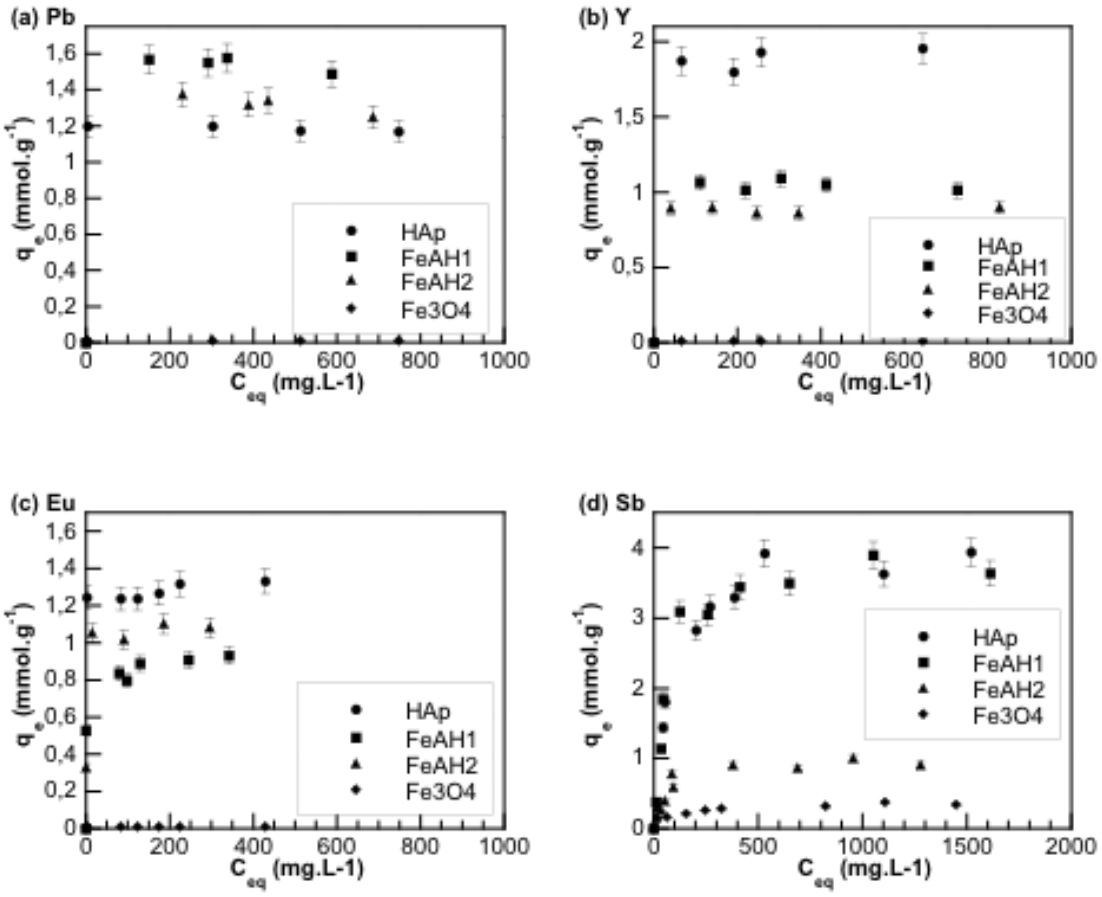

Fig. 6

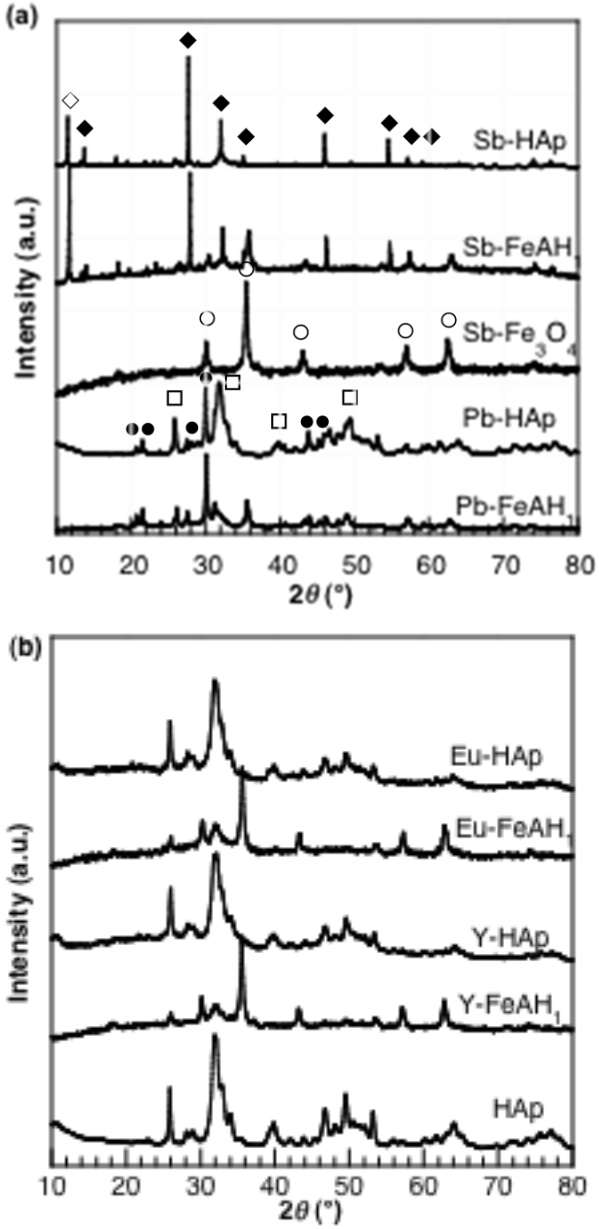
(a)
Sb-HAp
Sb-FeAH1
Sb-Fe3O4
Pb-HAp
Pb-FeAH1
Intensity (a.u.)
10 20 30 40 50 60 70 80
2θ (°)
(b)
Eu-HAp
Eu-FeAH1
Y-HAp
Y-FeAH1
HAp
Intensity (a.u.)
10 20 30 40 50 60 70 80
2θ (°)

Fig. 7

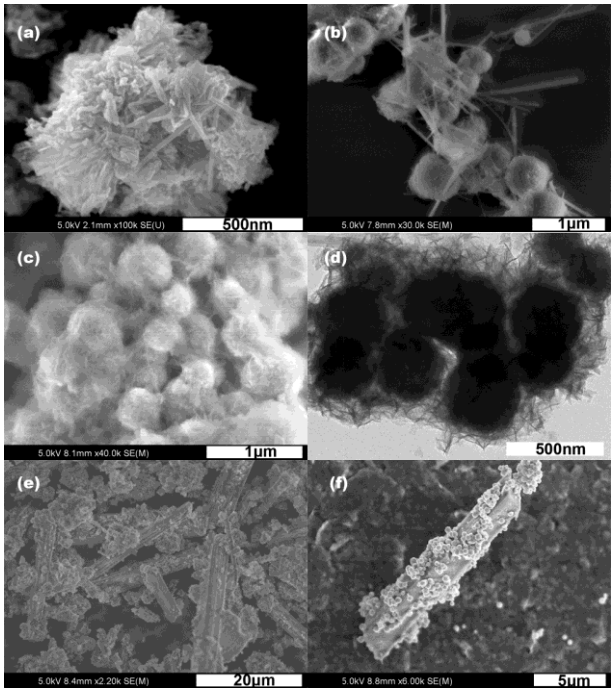
(a)
5.0kV 2.1mm x100k SE(U)
500nm
(b)
5.0kV 7.8mm x30.0k SE(M)
1μm
(c)
5.0kV 8.1mm x40.0k SE(M)
1μm
(d)
500nm
(e)
5.0kV 8.4mm x2.20k SE(M)
20μm
(f)
5.0kV 8.8mm x6.00k SE(M)
5μm

Fig. 8